



Active sites over CuO/CeO₂ and inverse CeO₂/CuO catalysts for preferential CO oxidation

Shanghong Zeng ^{a,b}, Yan Wang ^a, Suping Ding ^a, Jesper J.H.B. Sattler ^b, Elena Borodina ^b, Lu Zhang ^a, Bert M. Weckhuysen ^b, Haiquan Su ^{a,*}

^a Inner Mongolia Key Laboratory of Chemistry and Physics of Rare Earth Materials, School of Chemistry and Chemical Engineering, Inner Mongolia University, Hohhot 010021, PR China

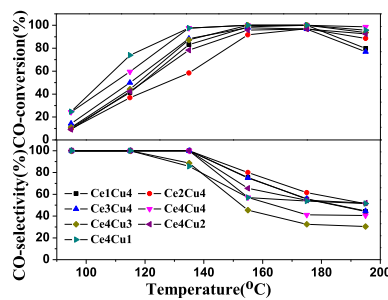
^b Inorganic Chemistry and Catalysis Group, Debye Institute for Nanomaterials Science, Utrecht University, Universiteitsweg 99, 3584 CA Utrecht, The Netherlands



HIGHLIGHTS

- CuO/CeO₂ and inverse CeO₂/CuO were prepared by surfactant-templated method.
- CuO/CeO₂ is ink-bottle-like pores and CeO₂/CuO has narrow slit-like pores.
- Lattice oxygen can make a significant contribution to the CO-PROX reaction.
- Ce4Cu4 and Ce4Cu1 catalysts exhibit best resistance against H₂O and CO₂.
- Resistance is related to BET surface area, crystallite sizes and reduction behavior.

GRAPHICAL ABSTRACT



ARTICLE INFO

Article history:

Received 29 October 2013

Received in revised form

17 January 2014

Accepted 21 January 2014

Available online 31 January 2014

Keywords:

Copper–ceria catalysts

Hydrogen

Active site

Preferential CO oxidation

ABSTRACT

A series of CuO/CeO₂ and inverse CeO₂/CuO catalysts are prepared by the surfactant-templated method and characterized via XRD, HRTEM, H₂-TPR, SEM, XPS, *in situ* XRD, *in situ* UV–Vis and N₂ adsorption–desorption techniques. It is found that there are two kinds of surface sites in the CuO–CeO₂ system, including CuO surface sites for CO chemisorption and CeO₂ surface sites with oxygen vacancies for oxygen sorption. The active sites for CO oxidation are located on the contact interface of two-kind surface sites and the lattice oxygen can make a significant contribution to the CO-PROX reaction. The resistance to H₂O and CO₂ is related to BET surface area, the crystallite sizes of CuO and the reduction behavior of catalysts. The Ce4Cu4 and Ce4Cu1 catalysts exhibit the best resistance against H₂O and CO₂.

© 2014 Elsevier B.V. All rights reserved.

1. Introduction

Hydrogen as a clean energy has attracted more and more attention due to the pressure from energy crisis, air pollution and climate change. However, the hydrogen feed that is produced from

steam reforming followed by the water–gas shift (WGS) reaction contains 0.5–2 vol % CO, which can poison the Pt electrodes of the proton-exchange membrane fuel cells (PEMFCs) [1–4]. Hence, it is essential to keep the CO concentration below 100 ppm level in the hydrogen entering the PEMFCs [5,6]. The preferential CO oxidation (CO-PROX) has been extensively accepted as one of the most cost-effective and straightforward techniques to achieve the acceptable CO concentration [4–7].

* Corresponding author.

E-mail address: haiquansu@yahoo.com (H. Su).

CuO–CeO₂ catalysts, as an alternative to noble metal catalysts, show excellent catalytic performance for eliminating CO in the hydrogen-rich gasses [5–13]. In 2000 Martínez-Arias and co-worker [14] proposed that CuO/CeO₂ is more active than CuO/ZrCeO₄ for CO oxidation, which can be attributed to the higher redox activity of the copper–support interface sites on the catalyst. Avgouropoulos et al. [15] prepared a series of CuO–CeO₂ catalysts by a co-precipitation method, and found that they are very active and exceptionally selective for the CO reaction and exhibit a good resistance toward H₂O and CO₂. Rodriguez et al. [16] first prepared the inverse TiO_{2-x}/Au(111) and CeO_{2-x}/Au(111) catalysts for the water–gas shift (WGS) reaction in 2007. Hornés et al. [6] reported an inverse CeO₂/CuO catalyst with wider CO conversion window and higher CO₂ selectivity in comparison with the classical CuO/CeO₂ catalyst in 2010, which is assigned to the maintenance of amount and properties of copper–ceria interfacial sites in this inverse system. Jia et al. [8] thought that the CO oxidation may occur at the interface between CuO and CeO₂ by comparison of the CuO/CeO₂ catalyst with 4.1 nm CuO crystallite size and the CeO₂/CuO catalyst with 4.0 nm CeO₂ crystallite size. In a previous study, it is reported that the CuO is the key active component in the CO-PROX reaction, and its reduction has a negative influence on the selective oxidation of CO. The advantage of the inverse CeO₂/CuO catalyst is that it still can provide sufficient CuO for CO oxidation below 200 °C in the hydrogen-rich gas mixtures [17].

Usually, the highly dispersed CuO is recognized as the active phase for CO oxidation [6,8,18]. The CeO₂ with the fluorite structure supplies the oxygen source by a Ce³⁺/Ce⁴⁺ redox couple, which can shift between CeO₂ and Ce₂O₃ depending on the atmosphere. In addition, the formation of oxygen vacancies due to doping is favorable for oxygen storage and mobility in the CeO₂ [19–24]. It is reported by Campbell [25] that the structure of surface oxygen vacancies is imperative to the chemical reactions because the vacancies can bind the adsorbates more strongly than other oxide sites and can also speed up their dissociation. It is obvious that there is a synergistic effect occurring at the interface of the CuO–CeO₂ catalysts and both CuO and CeO₂ play important roles in the CO oxidation reaction [7,8].

Although these previous studies give considerable insight into the nature of CO oxidation over the classical CuO/CeO₂ and inverse CeO₂/CuO catalysts, the search for the active sites is still in progress. In this work, we prepared a series of CuO/CeO₂ and inverse CeO₂/CuO catalysts in order to search the active sites and to investigate the decisive factors in this system.

2. Experimental

2.1. Catalyst preparation

The CuO/CeO₂ and inverse CeO₂/CuO catalysts were prepared by the surfactant-templated method [26]. 3.5 g Cetyltrimethyl ammonium bromide (CTAB) was dissolved in the aqueous solution, which consisted of 200 ml distilled water and 100 ml alcohol. The precursor salts of Cu(NO₃)₂·3H₂O and Ce(NO₃)₃·6H₂O (99.9%, Alfa Aesar) were added into the above aqueous solution according to different molar ratios. Then the solution of NaOH was added dropwise until the pH value of the mixture was adjusted to approximately 10.0. The precipitates were generated after adding alkali in the beakers, and they were aged for 14 h at 20°. Finally, the precipitates after washing and drying were calcined at 400 °C for 3 h in the air.

The obtained samples were composed of CeO₂ and CuO, and the catalysts were named in accordance to the molar ratios of CeO₂ and CuO. For example, the Ce1Cu4 catalyst indicated that the molar ratio of CeO₂ to CuO was 1:4. The other catalysts were marked as Ce2Cu4, Ce3Cu4, Ce4Cu4, Ce4Cu3, Ce4Cu2 and Ce4Cu1.

2.2. Catalyst characterization

2.2.1. X-ray diffraction

The powder X-ray diffraction (XRD) was performed on a Rigaku D/MAX 2500 X-ray diffractometer. The diffraction patterns of the samples were recorded with a Cu K α source ($\lambda \approx 0.1541$ nm) and a power setting of 36 kV and 20 mA in the range of 2θ between 10° and 80°. *In situ* time-resolved X-ray diffraction patterns were collected for the Ce1Cu4 and Ce4Cu1 samples on a D8 advance X-ray diffractometer with a Co K α source ($\lambda \approx 0.1789$ nm). The reduction experiments in the 50% H₂/He mixture were carried from 35 °C to 300 °C at a heating rate of 4.8 °C min⁻¹.

2.2.2. N₂ adsorption–desorption isotherms

The textural properties of the samples were determined by nitrogen physisorption at liquid nitrogen temperature using a Micromeritics Apparatus (Model ASAP2020). The surface area and pore size distribution were determined by the Brunauer–Emmett–Teller (BET) and the Barrett–Joyner–Halenda (BJH) methods, respectively.

2.2.3. Transmission electron microscopy

The transmission electron microscopy (TEM) images of the samples were collected with a FEI tecna F20 transmission electron microscope. The sample was dispersed into ethanol with the ultrasonic treatment for 10 min, and a drop of the suspension was placed on a copper grid for TEM observation.

2.2.4. Temperature-programmed reduction

The temperature-programmed reduction (TPR) was conducted on a Micromeritics Apparatus (AutoChemII2920). The 30 mg calcined catalyst was placed in a quartz reactor. The reactions were operated in a quartz reactor and the amount of H₂ consumption was measured by a thermal conductivity detector (TCD). The reduction profiles were collected in the 10% H₂/Ar gas mixture from room temperature to 900 °C. The flow rate of gas and heating rate were 50 ml min⁻¹ and 10 °C min⁻¹, respectively.

2.2.5. Scanning electron microscopy

The scanning electron microscopy (SEM) images of the samples were taken on a Hitachi S-4800 scanning electron microscope, using secondary electrons to form the images. The samples were coated with a thin layer of Pt before scanning.

2.2.6. X-ray photoelectron spectroscopy

The X-ray photoelectron spectra (XPS) of the catalysts were collected using a Physical Electronics Kratos Amicus spectrometer that was carried out under the UHV conditions with a tapered anode Mg K α radiation for the analyses of the core level signals of Cu 2p, Ce 3d and O 1s. During data processing of the XPS spectra, the binding energy values were calculated with the reference to the C 1s peak of contaminant carbon at 284.8–285.0 eV. The CasaXPS MFC Application software package was used for acquisition and data analysis.

2.2.7. Inductively coupled plasma-atomic emission spectrometry

The content of Ce and Cu was measured on an Inductively Coupled Plasma-Atomic Emission Spectrometer (ICP-AES) from American Varian Corporation.

2.2.8. In situ UV–Vis spectroscopy

In situ UV–Vis absorption measurements of the Ce1Cu4 and Ce4Cu1 catalysts were performed in the wavelength range of 200–1100 nm using a high-temperature UV–Vis probe produced by Avantes. The probe consisted of one excitation and one collection

fibers, which were connected to a Deuterium–Halogen light source and an Avaspec 2048 UV–Vis spectrometer. The reduction gasses were composed of 50% H₂ and 50% He. The flow rate of gas and heating rate were 30 ml min⁻¹ and 3 °C min⁻¹, respectively.

2.3. Catalytic performance tests

The catalytic oxidation of CO in hydrogen-rich gasses was carried in a quartz reactor inserted in a furnace. The reaction mixture consisted of 1% CO, 1% O₂ and 50% H₂ (volume fraction) with N₂ as balance gas. The space velocity was 40,000 ml g_{cat}⁻¹ h⁻¹. The reaction was operated between 35 °C and 215 °C. The bed temperature was measured by means of a thermocouple inserted in the furnace. Product and reactant analyses were conducted by a GC-2014C gas chromatograph. A 5 Å molecular sieve column was used to separate CO, O₂ and N₂. CO₂ was determined by a TDX column. Water was trapped before the gasses entering the GC and CO₂ was absorbed before entering the 5 Å molecular sieve. The water vapor (10 vol.%) and CO₂ (15 vol.%) was introduced into the reaction mixture when studying the effect of H₂O and CO₂ on the catalytic performance.

The conversion of CO (C_{CO}) and the selectivity for CO oxidation (S_{CO}) were calculated according to the equations (1) and (2) [2]:

$$C_{CO} = \frac{\text{inlet CO concentration} - \text{outlet CO concentration}}{\text{inlet CO concentration}} \times 100\% \quad (1)$$

$$S_{CO} = \frac{\text{inlet CO concentration} - \text{outlet CO concentration}}{2 \times (\text{inlet O}_2 \text{ concentration} - \text{outlet O}_2 \text{ concentration})} \times 100\% \quad (2)$$

3. Results and discussion

3.1. X-ray powder diffraction

Fig. 1 shows the XRD patterns of the CuO/CeO₂ and inverse CeO₂/CuO catalysts. The diffraction peaks are observed at 2θ of 28.68°, 34.61°, 47.55°, 56.51°, 59.12°, 69.59° and 77.01°, which can be assigned to the cubic fluorite CeO₂. The diffraction peaks appeared at 35.46°, 38.60°, 48.78°, 52.54°, 58.42°, 61.63°, 66.42°, 67.93°, 72.38° and 75.28°, correspond to the monoclinic CuO. For all

samples, the diffraction peaks of CeO₂ are broad, indicating that the CeO₂ is composed of the CeO₂ crystallites with small size. The diffraction peaks of CuO are narrow and sharp on the XRD patterns of Ce1Cu4, Ce2Cu4 and Ce3Cu4 catalysts (Fig. 1A–C), and it means that the CeO₂ is dispersed on the CuO supports with high crystallinity. There are weak and wide diffraction peaks of CuO over the Ce4Cu4 and Ce4Cu3 catalysts (Fig. 1D and E), which indicates that the crystallite sizes of CuO decrease in respect to the former three catalysts. For Ce4Cu1 and Ce4Cu2 catalysts (Fig. 1G and F), the XRD peaks of CuO cannot be detected due to low CuO content, or it is because that the CuO is highly dispersed on the CeO₂ supports [27,28].

Table 1 lists the average crystallite sizes calculated using the Scherrer formula from the line broadening of diffraction peaks of CeO₂ and CuO. In all catalysts, the crystallite size of CeO₂ is <=5 nm. The difference in the crystallite size of the directions (d_{111} , d_{220} , d_{311}) reveals the presence of anisotropy in the CeO₂ phase [18,26]. The Ce2Cu4 and Ce3Cu4 are less anisotropic than the other catalysts. In addition, the average crystallite sizes of CuO gradually decrease with the increase of CeO₂ content. As shown in Table 1, the lattice parameter of CeO₂ over the Ce1Cu4 catalyst does not change in comparison to pure CeO₂ (5.418 Å), indicating that Cu²⁺ does not replace Ce⁴⁺ in the CeO₂ crystal lattice. With the increase of CeO₂ content, the cell parameter of CeO₂ over the other catalysts exhibits little shrinkage, indicating that the partial Cu²⁺ enters into the crystal lattice of CeO₂ because the radius of Cu²⁺ (72 pm) is smaller than that of Ce⁴⁺ (92 pm) [17]. It is obvious that it is easy for Cu²⁺ to enter the crystal lattice of CeO₂, which is closely associated with the formation of oxygen vacancies [11].

3.2. Nitrogen physisorption analysis

Fig. 2 shows N₂ adsorption–desorption isotherms and BJH pore size distribution curves of the CuO/CeO₂ and inverse CeO₂/CuO catalysts. It can be seen that they all are type-IV isotherms according to the IUPAC classification, which correspond to typical mesoporous solids. The pore structure is related to the shape of hysteresis loop on the adsorption–desorption isotherm. As shown in Fig. 2, the Ce4Cu4, Ce4Cu3, Ce4Cu2 and Ce4Cu1 catalysts present hysteresis loops with a triangular shape and steep desorption branch, suggesting the presence of pores with narrow mouth and wide body (often referred to as ink-bottle-like pores). For Ce1Cu4, Ce2Cu4 and Ce3Cu4 catalysts, the hysteresis loops correspond to the narrow slit-like pores [29,30]. The maximum of BJH pore size distribution curves shifts to larger pore diameter with increasing CeO₂ content, which prove the above inferences. It means that the CuO/CeO₂ and inverse CeO₂/CuO catalysts have different pore size distributions. The CuO/CeO₂ catalysts have wide and ink-bottle-like pores and the inverse CeO₂/CuO catalysts have narrow slit-like pores.

Table 1 also includes the BET surface area and pore volume of the CuO/CeO₂ and inverse CeO₂/CuO catalysts. The general trend is that the BET surface area of the catalysts increases with the increase of CeO₂ content, suggesting that the CuO/CeO₂ catalysts have larger BET surface area than the inverse CeO₂/CuO catalysts, which is closely associated with the composition of the catalysts. In addition, the pore volume of the CuO/CeO₂ catalysts is also larger than that of the inverse CeO₂/CuO catalysts, which is related with BET surface area and pore distribution.

3.3. Transmission electron microscopy

TEM measurements were performed in order to complement the structural analyses of the CuO/CeO₂ and inverse CeO₂/CuO catalysts. Fig. 3 illustrates the images of the representative catalysts

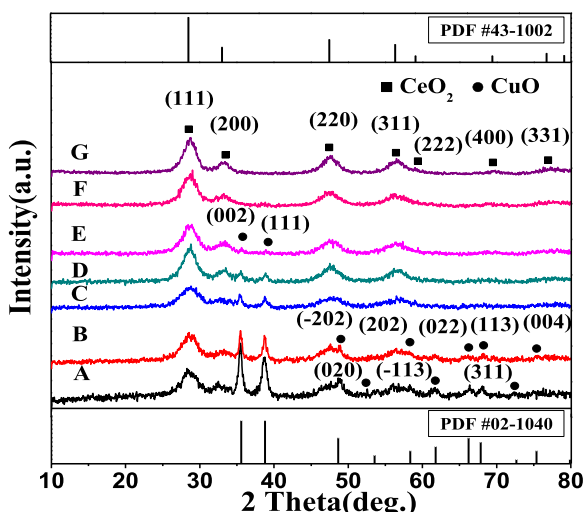


Fig. 1. XRD patterns of the catalysts: (A) Ce1Cu4; (B) Ce2Cu4; (C) Ce3Cu4; (D) Ce4Cu4; (E) Ce4Cu3; (F) Ce4Cu2; (G) Ce4Cu1.

Table 1

Physicochemical properties of CuO/CeO₂ and CeO₂/CuO catalysts.

Catalyst	Ce/Cu (molar ratio)	Crystallite size of CeO ₂ ^a (nm)			Crystallite size of CuO ^b (nm)	Lattice parameter (Å) ^c	S _{BET} (m ² g ⁻¹)	Pore volume (cm ³ g ⁻¹)
		d (111)	d (220)	d (311)				
Ce1Cu4	1:4	3.7	4.1	3.5	19.1	5.4181	102.0 (61.7) ^d	0.25632
Ce2Cu4	2:4	3.8	3.7	3.4	15.7	5.4125	132.4 (103.7) ^d	0.29764
Ce3Cu4	3:4	3.6	3.2	3.9	13.7	5.3610	131.8 (118.4) ^d	0.18632
Ce4Cu4	4:4	4.3	3.6	3.9	9.1	5.3645	198.3 (61.2) ^d	0.37066
Ce4Cu3	4:3	4.0	3.4	3.3	8.7	5.3361	185.7 (140.2) ^d	0.36906
Ce4Cu2	4:2	4.3	3.5	3.6	—	5.3941	192.7 (92.8) ^d	0.33775
Ce4Cu1	4:1	4.7	3.8	5.0	—	5.3579	205.8 (124.8) ^d	0.59965

^a Calculated from the Scherrer equation according to the diffraction peak of CeO₂.

^b Calculated from the Scherrer equation according to the [002] diffraction peak of CuO.

^c For fluorite phase.

^d BET surface area of the used catalysts (space velocity = 80,000 ml g_{cat}⁻¹ h⁻¹).

(Ce1Cu4, Ce4Cu2 and Ce4Cu1) examined by TEM, HRTEM and Electron diffraction patterns (ED patterns). For Ce1Cu4 catalyst, the CeO₂ crystallites (about 3–4 nm) gather into many small clusters, which are dispersed on the bulk CuO with high crystallinity (Fig. 3A1 and A2), indicating that the Ce1Cu4 catalyst is inverse configuration. It is accordant with the results of XRD measurements. For Ce4Cu2 and Ce4Cu1 catalysts, the CuO particles cannot be observed from HRTEM images (Fig. 3B2 and C2), implying that copper may be well-dispersed on the samples, or copper may be embedded in the lattice of ceria which can produce oxygen vacancies [11,31]. Moreover, the electron diffraction (ED) data of Ce4Cu2 and Ce4Cu1 catalysts show nearly pure CeO₂-type reflections. In other words, the CeO₂ particles consist of the CeO₂ crystallites with 3–5 nm sizes, and the CuO is highly dispersed on the CeO₂ particles or enters into the lattice of CeO₂ supports. They are the classical CuO/CeO₂ catalysts, which is also compatible with the XRD analysis.

3.4. TPR measurements

Fig. 4 shows TPR profiles of the CuO/CeO₂ and inverse CeO₂/CuO catalysts. Overlapping reduction peaks are observed in the 80–280 °C range, suggesting that there are at least two types of copper species (Fig. 4A). In the case of Ce4Cu4 (Fig. 4B), the signal at 100–200 °C is composed of three overlapping peaks (denoted as α , β and γ), corresponding to three types of copper species. The reduction peak at low temperature (α peak) corresponds to the reduction of highly dispersed CuO, the reduction peak at moderate temperature

(β peak) is assigned to the reduction of CuO in the lattice of ceria, and the reduction peak at high temperature (γ peak) is attributed to the reduction of bulk CuO [17]. The same conclusion about highly dispersed and bulk CuO was also mentioned by Maciel [32], Kundakovic [33] and Avgouropoulos [34].

In Fig. 4, α has a low signal and γ peak has a high signal on the TPR profile of Ce1Cu4 catalyst, suggesting that the CuO mainly exists in the form of bulk CuO. The α , β and γ peaks are present on the TPR profiles of Ce2Cu4, Ce3Cu4, Ce4Cu4 and Ce4Cu3, which means that there are three types of copper species over these catalysts. For Ce4Cu2 and Ce4Cu1, the γ peaks disappear on the TPR profiles, indicating that no bulk CuO is present over these two catalysts, in agreement with the analyses of XRD and TEM measurements. In addition, there are two peaks in the magnification figure of TPR profiles from 330 °C to 750 °C (Fig. 4C), corresponding to the reduction of surface ceria and bulk ceria, respectively.

Table 2 lists the reduction temperature and the total hydrogen consumption of CuO peaks on the TPR profiles of the catalysts. The reduction peaks of highly dispersed CuO, CuO in the lattice of ceria and bulk CuO appear at about 130–140 °C, 140–200 °C and 180–230 °C, respectively. Moreover, the total hydrogen consumption of CuO peaks over the catalysts decrease with the decrease of CuO content. Several authors [6,8,35] proposed that the highly dispersed CuO is the key active component over the CuO/CeO₂ catalyst for CO-PROX. In 2010 Hornés et al. [6] reported that the inverse CeO₂/CuO catalyst can be used as an alternative to classical direct configuration (CuO/CeO₂ catalyst) for CO-PROX due to wider full CO conversion window and higher CO₂ selectivity, which is related to the limited reducibility of larger size CuO particles. Which one is key active component among highly dispersed CuO, CuO in the lattice of ceria and bulk CuO? Where is active site over CuO/CeO₂ and inverse CeO₂/CuO catalysts? It is obvious that the temperature range of high activity for CO-PROX is closely associated with that of CuO reduction. This will be discussed in detail in the section of catalytic performance.

3.5. Scanning electron microscopy

Fig. 5 shows SEM micrographs of the CuO/CeO₂ and inverse CeO₂/CuO catalysts. It is clear that the content has a great influence on the morphology and structure of the catalysts. In combination with the TEM images (Fig. 3A1), it can be seen that the Ce1Cu4 catalyst is block structure, and the sheet-like surface projections are the CeO₂ clusters. The Ce2Cu4, Ce3Cu4 and Ce4Cu4 catalysts are composed of small bulk particles and present heterogenous morphology. The particles of catalysts increase when the molar ratios of Ce/Cu exceed 4:3, indicating that CeO₂ easily gathers together to form the certain morphology. At the same time, the BET surface area of the catalysts increases with the increase of CeO₂

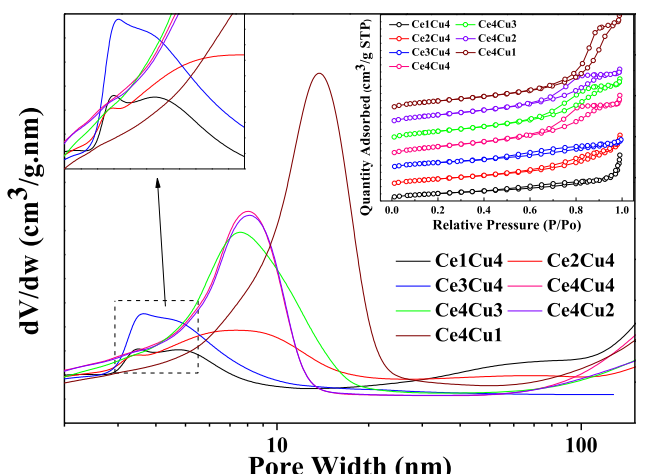


Fig. 2. N₂ adsorption–desorption isotherms and pore size distribution curves of the catalysts.

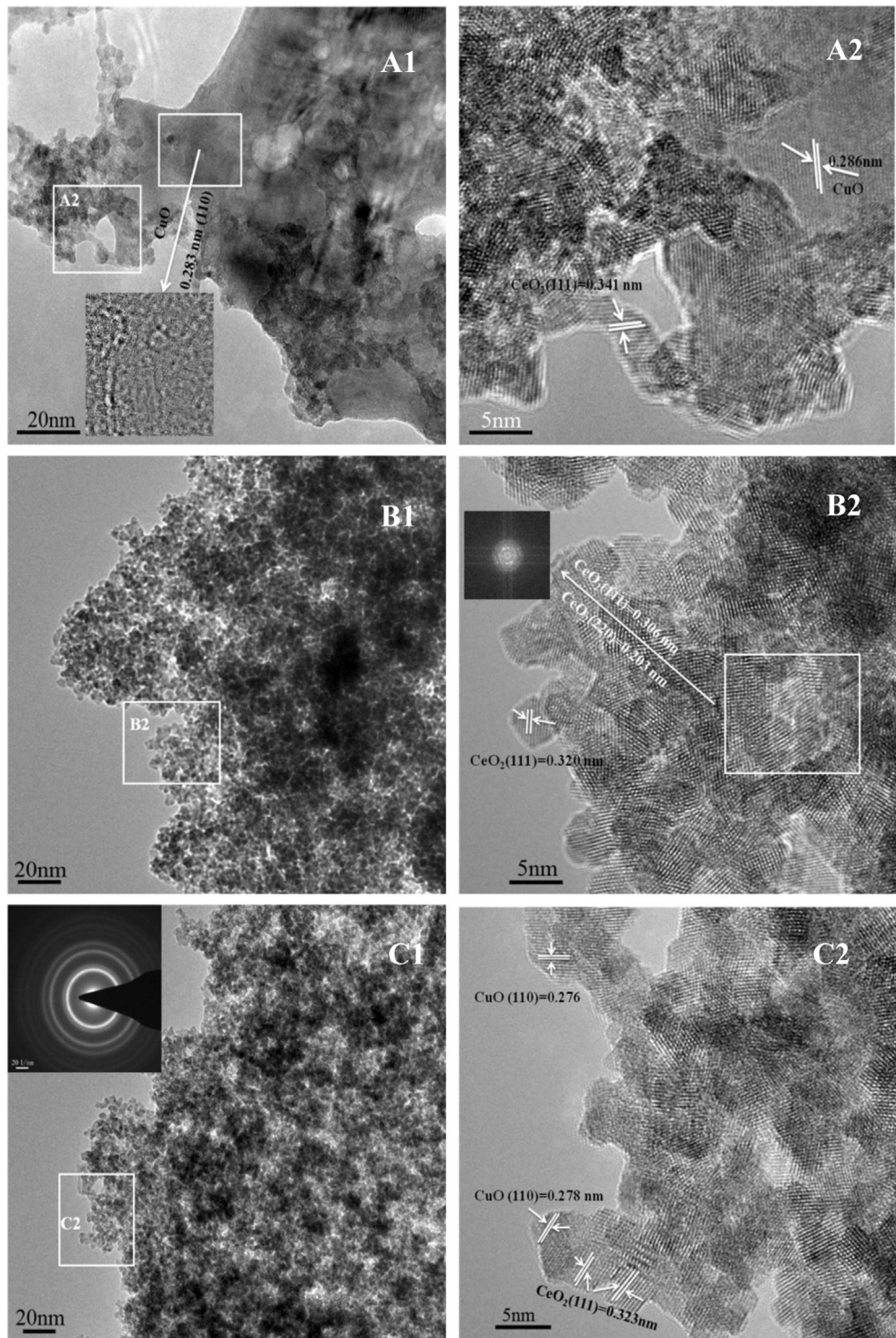


Fig. 3. TEM images of the catalysts: (A1) Ce1Cu4, (B1) Ce4Cu2, (C1) Ce4Cu1; HRTEM images of the catalysts: (A2) Ce1Cu4; (B2) Ce4Cu2; (C2) Ce4Cu1.

content, as mentioned in the analysis of textural property. It means that the massive CeO_2 formed is rich in the pores, which is composed of the 3–5 nm CeO_2 crystallites. The EDX analyses indicate that the CuO is not only distributed on the surface of CeO_2 supports, but also enters the ink-bottle-like pores for the classical CuO/CeO_2 catalysts. Similarly, the CeO_2 is located in the narrow slit-like pores of inverse CeO_2/CuO catalysts. This distribution is favorable for the increase of interfacial contact between CuO and CeO_2 .

3.6. XPS measurements

XPS measurements were performed in order to further examine the surface composition and the chemical state of the elements present in the CuO/CeO_2 and inverse CeO_2/CuO catalysts. As shown in Fig. 6A, a broad $\text{Cu} 2\text{p}_{3/2}$ signal, which is composed of two contributions at 933.1 and 934.8 eV, as well as a shake-up satellite in the 937–948 eV region are observed in the $\text{Cu} 2\text{p}$ spectra of the catalysts. It was reported that the higher $\text{Cu} 2\text{p}_{3/2}$ binding energy

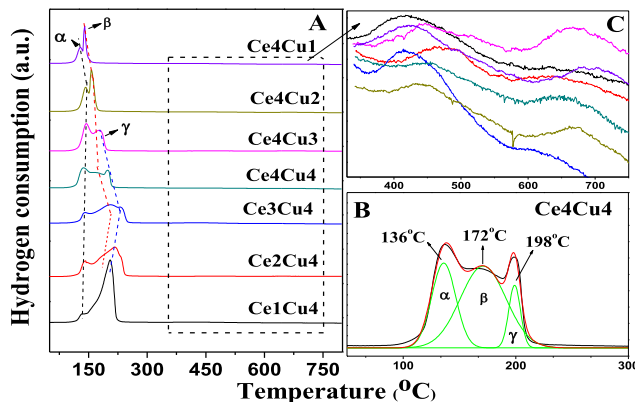


Fig. 4. (A) H₂-TPR profiles of the catalysts; (B) the TPR profiles of Ce4Cu4 at 50–300 °C; (C) the TPR profiles at 330–750 °C.

and the presence of the shake-up peak are two major XPS characteristics of Cu²⁺ species, while the lower Cu 2p3/2 binding energy and the absence of the shake-up peak are characteristic of Cu⁺ species [27,36,37]. Table 2 shows the intensity ratios of the satellite peaks to the principal peaks ($I_{\text{sat}}/I_{\text{pp}}$). It is known that this ratio is 0.57 for Cu²⁺ species [27,38]. Since the ratios of intensity are lower than 0.57, it is proposed that most of the copper species are in divalent oxidation state and a small amount is in lower valence state (Cu⁺) after calcination [38–40]. The presence of Cu⁺ species in the CuO/CeO₂ catalysts also has been reported by other researches [27,36,38].

Fig. 6B shows the Ce 3d spectra of the catalysts. The complex Ce 3d spectra are composed of eight peaks with the assignment defined in Fig. 6B (Ce4Cu4 as an example), which are attributed to four pairs of spin-orbit doublets. It is implied that the Ce³⁺ and Ce⁴⁺ are present in the CuO/CeO₂ and inverse CeO₂/CuO catalysts [41]. This is important because the presence of Ce³⁺ is believed to be related to the formation of oxygen vacancies, which can improve catalytic performance of the catalysts in the CO-PROX reaction [41].

The O1s spectra of the catalysts are displayed in Fig. 6C. The main peaks are centered at about 528.6 eV, and are assigned to the lattice oxygen of CeO₂ and CuO phases. The shoulder peaks at about 530.2 eV are attributed to the absorbed oxygen or oxygen in hydroxyl groups [37,38]. The mobility of oxygen in ceria is improved by the relative freedom movement of lattice oxygen due to the presence of defect sites (oxygen vacancies) from Cu substitutions, which is proved by XRD analyses. It is well known that high oxygen mobility can enhance the oxygen storage capacity and the reactivity of lattice oxygen, which are important to obtain a highly active catalyst for CO oxidation [42,43]. Fig. 6C also depicts the intensity of lattice oxygen with the change of CeO₂ content. The general trend of the lattice oxygen intensity is consistent with the order of

catalytic performance (Fig. 9), indicating that the lattice oxygen can make a significant contribution to the CO-PROX reaction.

Table 2 shows the intensity ratios of $I_{\text{Ce3d}}/(I_{\text{Cu2p}} + I_{\text{Ce3d}})$ and $I_{\text{Cu2p}}/(I_{\text{Cu2p}} + I_{\text{Ce3d}})$ (analysis depth < 2 nm) in the XPS spectra as a function of a relative evaluation of the dispersed copper and ceria species on the catalyst surface. It is interesting that these values are close to 0.50 for all catalysts. It is well known that the active components are rich on the catalyst surface for most of the supported catalysts, which can save the active components and improve the catalytic performance. It is obvious that neither CuO nor CeO₂ is the only active phase for CO-PROX. The approaching ratio can improve contact and interaction between CuO and CeO₂ on the surface. Either CuO dispersed on CeO₂ (classical CuO/CeO₂ catalyst), or CeO₂ dispersed on CuO (inverse CeO₂/CuO catalyst), are not all in order to increase their contact and interaction?

3.7. In situ time-resolved X-ray diffraction

Fig. 7 shows *In situ* time-resolved X-ray diffraction patterns of the Ce1Cu4 and Ce4Cu1 catalysts. For Ce1Cu4, the phase of copper oxide is observed at low temperature, but the diffraction peaks corresponding with metallic copper appear when the temperature increases to 158 °C, which means that CuO is reduced into metallic copper in the 50% H₂/He stream. At 190 °C, the copper oxide is completely reduced. For Ce4Cu1, the diffraction peak of CuO cannot be observed at low temperature, indicating that the CuO is highly dispersed on the CeO₂, which is in the agreement with the analysis of HRTEM. The phase of metallic copper appears when heating to 139 °C, which suggests that metallic copper is formed as the ordered crystallites. In addition, the intensity of CeO₂ diffraction peaks do not change when the samples are heated from 35 °C to 300 °C for the Ce1Cu4 and Ce4Cu1 catalysts, which means that the CeO₂ cannot be reduced before 300 °C. This is in agreement with the results of the TPR measurements.

As shown in Fig. 7, the CuO is directly reduced into metallic copper and no Cu⁺ intermediate is found during the reduction process for both the Ce1Cu4 and Ce4Cu1 catalysts. The same conclusion was also reported by Rodriguez [44] and Zheng [45]. It is well known that the gas–solid reduction reaction proceeds from the surface to the bulk, and the final reduction product is determined by the molar ratio of copper oxide to hydrogen. Rodriguez [44] has proposed that the system can reach a metastable states (MS) and react with hydrogen instead of forming Cu₂O during the reduction of CuO. It means that the flow rate of hydrogen should be limited if the formation of Cu₂O is expected, slowing the speed of reduction to allow an MS to Cu₂O transformation. In this measurement, the Ce1Cu4 and Ce4Cu1 catalysts were exposed to the substantial hydrogen, therefore the diffraction peaks of Cu₂O cannot be observed in Fig. 7.

Table 2
The redox behavior and surface compositional analysis of the catalysts.

Catalyst	Ce/(Cu + Ce) (molar ratio) ^a	Ce/(Cu + Ce) (molar ratio) ^b	H ₂ consumption (mmol g ⁻¹ _{cat})	Peak position (°C)			$I_{\text{sat}}/I_{\text{pp}}$	$I_{\text{Ce3d}}/(I_{\text{Cu2p}} + I_{\text{Ce3d}})$	$I_{\text{Cu2p}}/(I_{\text{Cu2p}} + I_{\text{Ce3d}})$
				α	β	γ			
Ce1Cu4	0.24	0.13	9.19	133	—	203	0.46	0.49	—
Ce2Cu4	0.38	0.56	7.40	136	189	222	0.53	0.50	—
Ce3Cu4	0.46	0.53	5.35	141	206	231	0.49	0.53	—
Ce4Cu4	0.53	0.65	5.08	136	172	198	0.51	0.51	0.49
Ce4Cu3	0.56	0.56	4.46	141	169	180	0.48	—	0.45
Ce4Cu2	0.69	0.65	3.80	136	157	—	0.49	—	0.49
Ce4Cu1	0.85	0.80	1.98	128	140	—	0.43	—	0.49

^a Calculated by ICP.

^b Calculated by EDX analyses of the SEM micrographs.

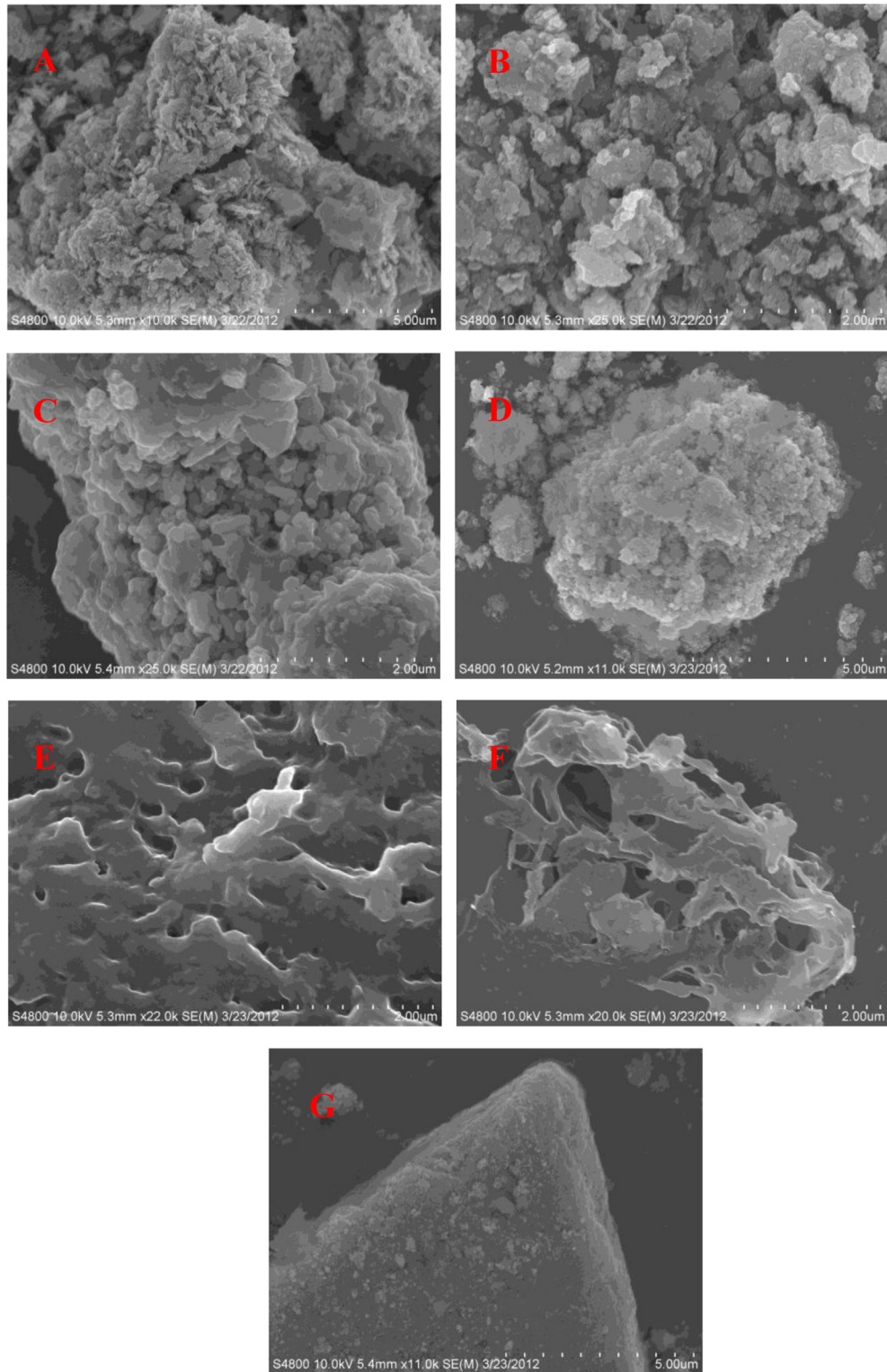


Fig. 5. SEM images of the catalysts: (A) Ce1Cu4; (B) Ce2Cu4; (C) Ce3Cu4; (D) Ce4Cu4; (E) Ce4Cu3; (F) Ce4Cu2; (G) Ce4Cu1.

3.8. In situ UV–Vis spectra

Fig. 8 shows the UV–Vis-diffuse spectra of the Ce1Cu4 and Ce4Cu1 catalysts. Generally, pure CuO presents a wide absorption peak centered at about 380 nm [46]. Pure CeO₂ has three absorption features at 226, 280 and 345 nm, respectively corresponding to

O²⁻ → Ce³⁺ and O²⁻ → Ce⁴⁺ charge transfer transitions as well as inter band transitions in CeO₂ [28]. For Ce1Cu4, the absorption bands appeared at 245 and 255 nm are attributed to O²⁻ → Ce³⁺ and O²⁻ → Ce⁴⁺ charge transfer transitions. The absorption bands at 400–550 nm are assigned to emission and absorption of one photon by Cu⁺ complexes and/or absorption from the conduction

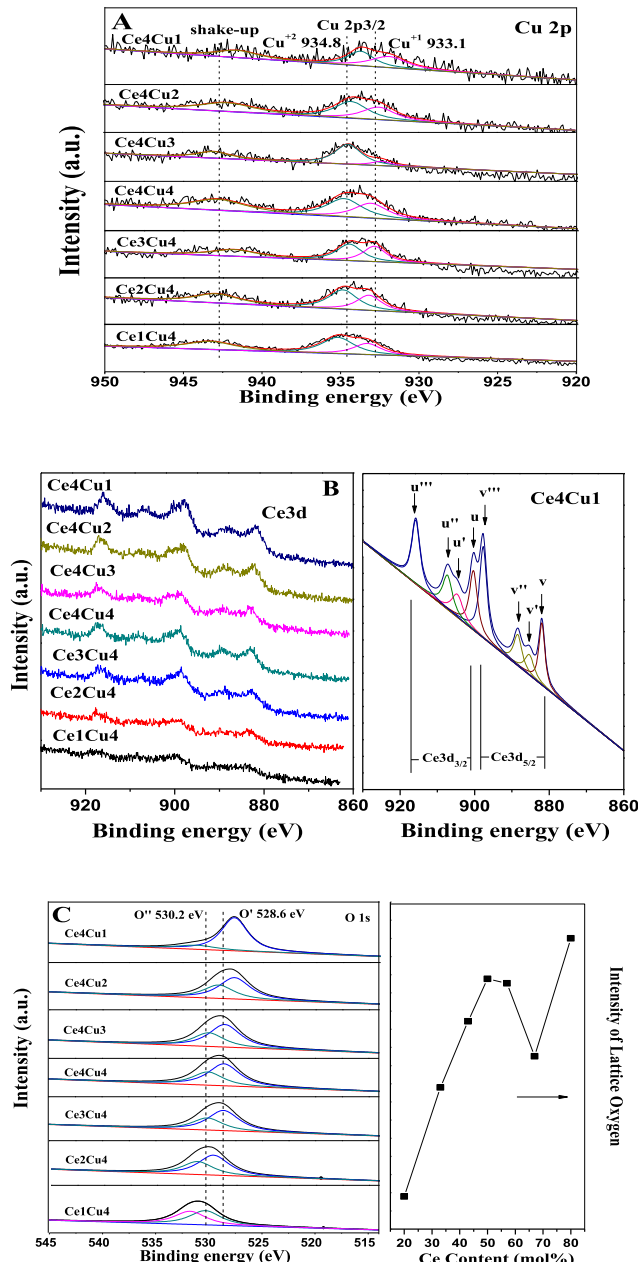


Fig. 6. XPS spectra of the CuO/CeO₂ and inverse CeO₂/CuO catalysts: (A) Cu 2p; (B) Ce 3d; (C) O 1s.

band of metallic copper [28]. The change of spectra cannot be observed from 55 to 295 °C in the H₂/He mixture because the copper species has weaker intense band in compare with CeO₂.

For Ce4Cu1, the absorption bands appear at 237 and 260 nm with an absorption edge around 400 nm, attributed to the characteristic of fluorite structure CeO₂ [47]. Among them, the absorption at 237 nm corresponds to O²⁻ → Ce³⁺ charge transfer transitions, which is closely associated with the presence of oxygen vacancies. The absorption bands at 400–550 nm are attributed to the adsorption of Cu⁺ and/or Cu⁰ species. It is reported that the location and intensity of adsorption bands depend on ion density and chemical environment [48]. It is noteworthy that the absorption bands at 237 nm shift lower wavelength and the intensities of absorption bands at 260 nm increase with the increase of temperature from 55 to 600 °C, which may result from the reduction of surface ceria. It is compatible with the result of TPR measurements.

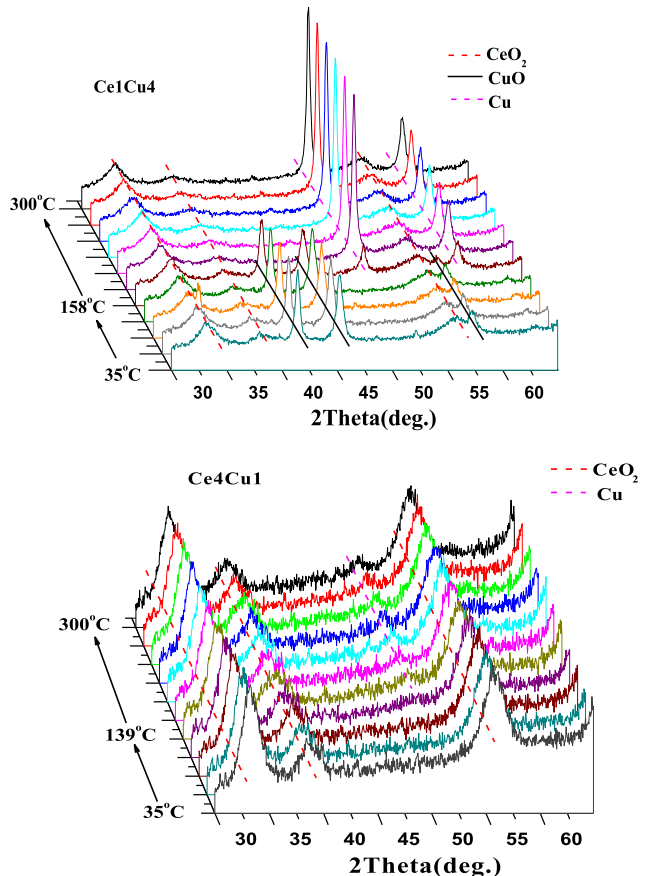


Fig. 7. *In situ* X-ray diffraction patterns of Ce1Cu4 and Ce4Cu1 catalysts from 35 to 300 °C in 50% H₂/He mixture.

3.9. Catalytic performance

3.9.1. Preferential CO oxidation

The catalytic performance of the catalysts was evaluated in the CO-PROX reaction within the temperature range from 35 °C to 215 °C, using a mixture gas (1% CO, 1% O₂, 50% H₂ and N₂ balance). Fig. 9 illuminates the temperature dependency of the CO conversion and selectivity over the CuO/CeO₂ and inverse CeO₂/CuO catalysts. It can be seen that all the catalysts exhibit similar levels of conversion except the Ce1Cu4. The Ce1Cu4 catalyst can achieve 100% CO conversion between 115 °C and 175 °C, which presents lower activities at low and high temperatures in comparison to the other catalysts. For all catalysts, the selectivity to CO₂ is above 80% below 115 °C. After 115 °C, the selectivity rapidly decreases with increasing reaction temperature. Furthermore, the performance tests were also carried out at space velocity of 80,000 ml g_{cat}⁻¹ h⁻¹ in order to discriminate the activities of the catalysts. As shown in Fig. 10, the Ce4Cu4 and Ce2Cu4 catalysts exhibit better low-temperature activity and the Ce4Cu1 and Ce4Cu3 catalysts display better high-temperature activity. It is obvious that the high intensity of lattice oxygen is favorable for catalytic performance, as mentioned in the XPS measurements. The BET surface area of the used samples was measured by nitrogen physisorption after CO-PROX reaction (space velocity = 80,000 ml g_{cat}⁻¹ h⁻¹). It can be observed in Table 1 that the Ce3Cu4, Ce4Cu3 and Ce4Cu1 catalysts still maintain high BET surface area after the reaction.

In our previous study [17], the inverse CeO₂/CuO catalysts prepared by the hydrothermal method can attain 100% CO conversion between 135 °C and 195 °C. It is obvious that the catalytic

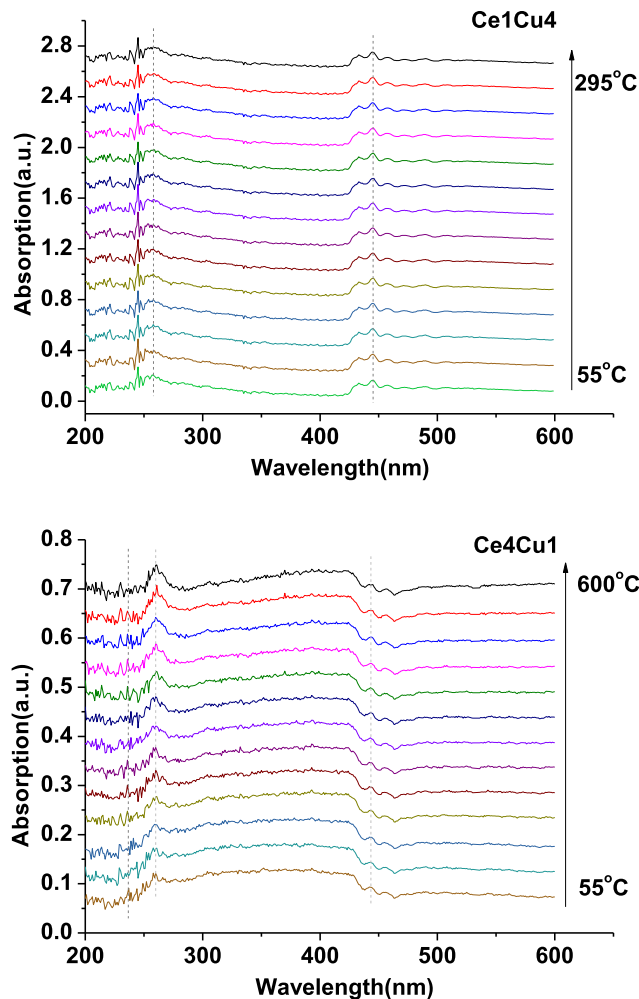


Fig. 8. *In situ* UV-Vis spectra of the Ce1Cu4 and Ce4Cu1 catalysts in the H₂/He mixture.

performance of the catalysts synthesized by the surfactant-templated method is better than that of the catalysts prepared by the hydrothermal route. As shown in Table 1, the CuO/CeO₂ and inverse CeO₂/CuO catalysts in this work possess larger BET surface area and

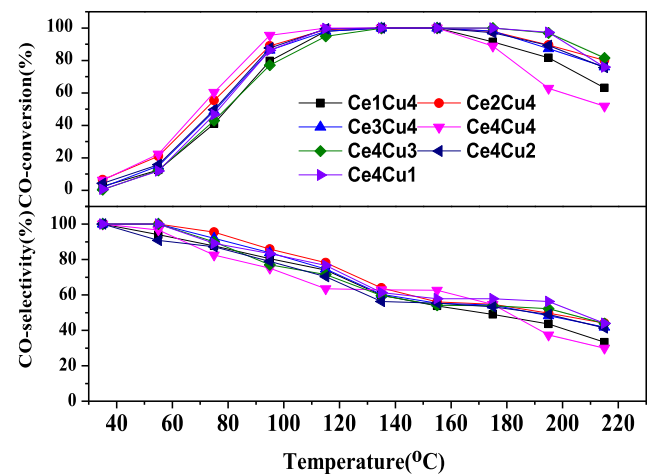


Fig. 10. CO conversion and selectivity over the catalysts ([CO]in = 1%; [O₂]in = 1%; [H₂]in = 50%; N₂ balance; space velocity = 80,000 ml g_{cat}⁻¹ h⁻¹).

pore volume compared with the inverse CeO₂/CuO catalysts prepared by the hydrothermal method [17], which is closely associated with the nucleation and growth of the CuO–CeO₂ catalysts. The catalysts synthesized by surfactant-templated method have smaller crystallite sizes of CeO₂ and CuO, and the hydrothermal method is favorable for the nucleation and growth of CeO₂ and CuO.

It is commonly accepted that the highly dispersed CuO is the active phase for CO oxidation until the inverse CeO₂/CuO catalysts appear in the field of vision [6,8]. Jia et al. [8] thought that the reaction may occur at the interface of CuO–CeO₂ and the CuO–CeO₂ catalyst for CO oxidation is structure-sensitive by comparing CuO/CeO₂ and CeO₂/CuO catalysts. As is known, both pure CuO and pure CeO₂ can achieve 100% CO conversion at about 230 °C and 300 °C, respectively [8,43]. The superior performance is shown at low temperature only when CuO and CeO₂ are combined together. If the highly dispersed CuO is the active phase for CO oxidation, the highly dispersed CuO supported on other supports should present good performance. As mentioned in the literature, the CuO/SiO₂ and CuO/γ-Al₂O₃ catalysts are less active than the pure CuO [26]. It is obvious that both CuO and CeO₂ have contributions for CO oxidation, and their contact and interaction improve low-temperature activity [49].

Liu and Flytzani-Stephanopoulos [50] thought that Cu⁺ species are stabilized by the interaction between CuO and CeO₂. Moreover, the Cu⁺ species supply surface sites for CO chemisorption and the CeO₂ provides oxygen via a fast Ce⁴⁺/Ce³⁺ redox cycle. As mentioned above, pure CuO and pure CeO₂ are active for CO oxidation, indicating that both CuO and CeO₂ also can supply surface sites for CO chemisorption, especially CuO, which can achieve 100% CO conversion at lower temperature in comparison with CeO₂. The study of the mechanism for CO oxidation over the CuO–CeO₂ catalysts indicates that the superoxide species or lattice oxygen atoms formed on ceria directly participate in the CO oxidation instead of gas phase oxygen [8]. As is mentioned in the analysis of the XPS measurements, the concentration of lattice oxygen is closely related to the catalytic performance. In other words, there are two kinds of surface sites in the system, including CuO surface sites for CO chemisorption and CeO₂ surface sites with oxygen vacancies that serve as an oxygen supply. Therefore, the active sites for CO oxidation are located at the interface of CuO and CeO₂. That is why the catalysts cannot present superior performance when one of CuO and CeO₂ is at a low content. It is reported that the activity significantly improves when the CuO content of the CuO/CeO₂ increases until 12.0 mol% [26]. Our previous study shows that low

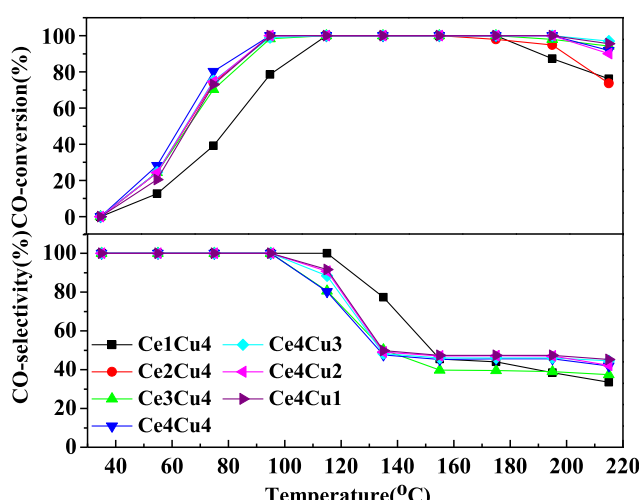


Fig. 9. CO conversion and selectivity over the catalysts ([CO]in = 1%; [O₂]in = 1%; [H₂]in = 50%; N₂ balance; space velocity = 40,000 ml g_{cat}⁻¹ h⁻¹).

CeO_2 content influences catalytic performance of the CeO_2/CuO catalyst, and the inverse catalysts show better catalytic performance when the CeO_2 content increases to 33.0 mol% [17,51].

The highly dispersed CuO is regarded to be the active phase, because it is easily reduced at low temperature (below 100 °C). The occurrence of its reduction stimulates the $\text{Ce}^{4+}/\text{Ce}^{3+}$ redox cycle, therefore the catalytic performance is improved over the catalysts. Our previous study shows that the CuO/CeO_2 catalysts have a better low-temperature activity than the CeO_2/CuO catalyst due to the presence of the highly dispersed CuO [51], which is in agreement with our findings here. As reported by Jia et al. [8], the enhanced activity is attributed to a higher density of chemisorbed CO on the active sites for the larger CuO crystallite. However, the wider full CO conversion window and the higher CO_2 selectivity over the inverse CeO_2/CuO catalyst comes at the expense of a decrease of low-temperature activity due to the absence of highly dispersed CuO in comparison to the CuO/CeO_2 catalyst. As shown in Fig. 9, both the CuO/CeO_2 and inverse CeO_2/CuO catalysts cannot achieve 100% CO conversion when the temperature reaches 190 °C due to competitive H_2 oxidation, which is in agreement with the results of Jia and Hornés [6,8].

As mentioned above, the catalysts in this work exhibit similar levels of conversion with the exception of Ce1Cu4. The weak low-temperature activity of Ce1Cu4 (below 115 °C) is attributed to the lack of highly dispersed CuO because the CuO mainly presents in the form of bulk CuO. In addition, the inverse Ce1Cu4 and Ce2Cu4 catalysts do not present higher activity at high temperature (above 175 °C) than the other catalysts because the larger CuO particles are easily reduced over the Ce1Cu4 and Ce2Cu4 catalysts. It is noteworthy that the BET surface area is another important factor for catalytic activity. The Ce4Cu4, Ce4Cu3, Ce4Cu2, and Ce4Cu1 catalysts have large BET surface area, therefore they all present good catalytic performance and wide full CO conversion window. Among them, the Ce4Cu3 and Ce4Cu1 catalysts still maintain high BET surface area after the reaction.

To be a conclusion, there are three important factors for the $\text{CuO}-\text{CeO}_2$ system, which are composition, content and BET surface area. Whether it is classical CuO/CeO_2 or inverse CeO_2/CuO catalyst all have to consider these three factors in order to achieve high activity and wide full CO conversion window. The key issue is to select appropriate chemical composition and preparation method to obtain a catalyst with a high BET surface area.

3.9.2. Effect of the addition of H_2O and CO_2 on the CO-PROX

It is essential to test the performance of the catalysts with H_2O and CO_2 present in the stream because the hydrogen-rich gasses obtained from the reforming process usually contain both 10% H_2O and 15% CO_2 . Fig. 11 shows CO conversion and selectivity over the CuO/CeO_2 and inverse CeO_2/CuO catalysts when both H_2O and CO_2 were added to the gas stream. It is observed that the activity of all catalysts is substantially inhibited by the comparison with Fig. 9. The existence of the H_2O and CO_2 shifts the temperature for CO total conversion to higher temperature. Moreover, the reaction for CO total conversion occurs at the narrow region of temperature. Gurbani et al. [52] proposed that the competitive adsorption of CO_2 and CO on the oxides and the blockage of the active sites by water vapor are two probable reasons for the decrease of the activity under the presence of H_2O and CO_2 . It is possible that H_2O and CO_2 influence the adsorption of CO and O₂ at lower temperature, which lead to the decrease of catalytic activity of the as-prepared catalysts at lower temperature. It is called as the poisoning effect of H_2O and CO_2 on the CO-PROX catalysts.

Among the catalysts, the Ce4Cu4 and Ce4Cu1 catalysts exhibit better catalytic performance in comparison with the other catalysts under the presence of H_2O and CO_2 in the stream. As shown in

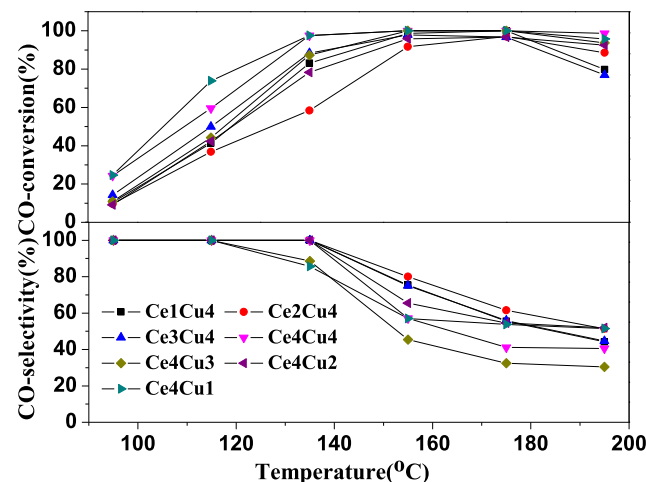


Fig. 11. CO conversion and selectivity over the catalysts ($[\text{CO}]_{\text{in}} = 1\%$; $[\text{O}_2]_{\text{in}} = 1\%$; $[\text{H}_2]_{\text{in}} = 50\%$; $[\text{H}_2\text{O}]_{\text{in}} = 10\%$; $[\text{CO}_2]_{\text{in}} = 15\%$; N_2 balance; space velocity = 40,000 ml g_{cat} h⁻¹).

Table 1, the Ce4Cu4 and Ce4Cu1 catalysts possess high BET surface area, suggesting that the resistance ability to H_2O and CO_2 may be closely related the BET surface area. In addition, the Ce4Cu3 and Ce4Cu2 show better activity than the Ce1Cu4, Ce3Cu4 and Ce2Cu4 at higher temperature and they also have high BET surface area, which further prove the BET surface area is an important factor for the CuO/CeO_2 or inverse CeO_2/CuO catalysts.

Furthermore, it can be seen from Table 1 and Fig. 4 that there are CuO with big crystallite sizes in the Ce1Cu4, Ce3Cu4 and Ce2Cu4 catalysts. As shown in Fig. 11, they have weaker resistance to H_2O and CO_2 than other samples, suggesting that the resistance to H_2O and CO_2 is also associated with the crystallite sizes of CuO and the reduction behavior of catalysts.

4. Conclusions

A series of CuO/CeO_2 and inverse CeO_2/CuO catalysts were prepared by the surfactant-templated method. It is found that the CuO/CeO_2 and inverse CeO_2/CuO catalysts have different pore size distributions. The CuO/CeO_2 catalysts have wide and ink-bottle-like pores and the inverse CeO_2/CuO catalysts have narrow slit-like pores. In the $\text{CuO}-\text{CeO}_2$ system, there are two kinds of surface sites, namely CuO surface sites for CO chemisorption and CeO_2 surface sites with oxygen vacancies for oxygen sorption. The active sites for CO oxidation are located on the contact interface of two-kind surface sites and the lattice oxygen can make a significant contribution to the CO-PROX reaction. The resistance to H_2O and CO_2 is related to BET surface area, the crystallite sizes of CuO and the reduction behavior of catalysts. The Ce4Cu4 and Ce4Cu1 catalysts exhibit the best resistance against H_2O and CO_2 .

Acknowledgments

The authors would like to acknowledge the National Natural Science Foundation of China (grant no. 21066004, 21061008).

References

- [1] E. Morettia, L. Storaroa, A. Talona, M. Lenardaa, P. Riello, R. Frattini, Appl. Catal. B: Environ. 102 (2011) 627–637.
- [2] J. Xu, X.C. Xu, L. Ouyang, X.J. Yang, W. Mao, J.J. Su, Y.F. Han, J. Catal. 287 (2012) 114–123.
- [3] L. Barrio, M. Estrella, G. Zhou, W. Wen, J.C. Hanson, A.B. Hungría, A. Hornés, M. Fernández-García, A. Martínez-Arias, J.A. Rodriguez, J. Phys. Chem. C. 114 (2010) 3580–3587.

- [4] Y. Kobayashi, K. Omata, M. Yamada, *Ind. Eng. Chem. Res.* 49 (2010) 1541–1549.
- [5] A.L. Cámera, A. Kubacka, Z. Schay, Zs. Koppány, A. Martínez-Arias, *J. Power Sources* 196 (2011) 4364–4369.
- [6] A. Hornés, A.B. Hungría, P. Bera, A. López Cámera, M. Fernández-García, A. Martínez-Arias, *J. Am. Chem. Soc.* 132 (2010) 34–35.
- [7] S.H. Zeng, Y. Wang, K.W. Liu, F.R. Liu, H.Q. Su, *Int. J. Hydrogen Energy* 37 (2012) 11640–11649.
- [8] A.P. Jia, S.Y. Jiang, J.Q. Lu, M.F. Luo, *J. Phys. Chem. C* 114 (2010) 21605–21610.
- [9] T. Caputo, L. Lisi, R. Pirone, G. Russo, *Ind. Eng. Chem. Res.* 46 (2007) 6793–6800.
- [10] J.L. Ayastuy, A. Gurbani, M.P. González-Marcos, M.A. Gutiérrez-Ortiz, *Ind. Eng. Chem. Res.* 48 (2009) 5633–5641.
- [11] D. Gamarra, G. Munuera, A.B. Hungría, M. Fernández-García, J.C. Conesa, P.A. Midgley, X.Q. Wang, J.C. Hanson, J.A. Rodríguez, A. Martínez-Arias, *J. Phys. Chem. C* 111 (2007) 11026–11038.
- [12] P. Djinović, J. Batista, B. Čehić, A. Pintar, *J. Phys. Chem. A* 114 (2010) 3939–3949.
- [13] Z.X. Yang, B.L. He, Z.S. Lu, K. Hermansson, *J. Phys. Chem. C* 114 (2010) 4486–4494.
- [14] A. Martínez-Arias, M. Fernández-García, O. Gálvez, J.M. Coronado, J.A. Anderson, J.C. Conesa, J. Soria, G. Munuera, *J. Catal.* 195 (2000) 207–216.
- [15] G. Avgouropoulos, T. Ioannides, H.K. Matralis, J. Batista, S. Hocevar, *Catal. Lett.* 73 (2001) 33–40.
- [16] J.A. Rodriguez, S. Ma, P. Liu, J. Hrbek, J. Evans, M. Pérez, *Science* 318 (2007) 1757–1760.
- [17] S.H. Zeng, W.L. Zhang, M. Sliwa, H.Q. Su, *Int. J. Hydrogen Energy* 38 (2013) 3597–3605.
- [18] M.F. Luo, Y.P. Song, J.Q. Lu, X.Y. Wang, Z.Y. Pu, *J. Phys. Chem. C* 111 (2007) 12686–12692.
- [19] F. Zamar, A. Trovarelli, C. de Leitenburg, G. Dolcetti, *J. Chem. Soc. Chem. Commun.* 9 (1995) 965–966.
- [20] F. Yang, J. Graciani, J. Evans, P. Liu, J. Hrbek, J.F. Sanz, J.A. Rodriguez, *J. Am. Chem. Soc.* 133 (2010) 3444–3451.
- [21] M. Nolan, S.C. Parker, G.W. Watson, *Surf. Sci.* 595 (2005) 223–232.
- [22] W. Liu, M. Flytzani-Stephanopoulos, *J. Catal.* 153 (1995) 304–316.
- [23] X.W. Liu, K.B. Zhou, L. Wang, B.Y. Wang, Y.D. Li, *J. Am. Chem. Soc.* 131 (2009) 3140–3141.
- [24] D.Y. Wang, Y.J. Kang, V. Doan-Nguyen, J. Chen, R. Küngas, N.L. Wieder, K. Bakhtutsky, R.J. Gorte, C.B. Murray, *Angew. Chem. Int. Ed.* 50 (2011) 4378–4381.
- [25] C.T. Campbell, C.H.F. Peden, *Science* 309 (2005) 713–714.
- [26] M.F. Luo, J.M. Ma, J.Q. Lu, Y.P. Song, Y.J. Wang, *J. Catal.* 246 (2007) 52–59.
- [27] G. Avgouropoulos, T. Ioannides, *Appl. Catal. A: Gen.* 244 (2003) 155–167.
- [28] V.D. Araújo, J.D.A. Bellido, M.I.B. Bernardi, J.M. Assaf, E.M. Assaf, *Int. J. Hydrogen Energy* 37 (2012) 5498–5507.
- [29] K.S.W. Sing, D.H. Everett, R.A.W. Haul, L. Moscou, R.A. Pierotti, J. Rouquerol, T. Siemieniewska, *Pure Appl. Chem.* 57 (1985) 603–619.
- [30] J.L. Cao, G.S. Shao, T.Y. Ma, Y. Wang, T.Z. Ren, S.H. Wu, Z.Y. Yuan, *J. Mater. Sci.* 44 (2009) 6717–6726.
- [31] J. Ciston, R. Si, J.A. Rodriguez, J.C. Hanson, A. Martínez-Arias, M. Fernández-García, Y. Zhu, *J. Phys. Chem. C* 115 (2011) 13851–13859.
- [32] C.G. Maciel, T. de F. Silva, L.P.R. Profeti, E.M. Assaf, J.M. Assaf, *Appl. Catal. A: Gen.* 431–432 (2012) 25–32.
- [33] Lj. Kundakovic, M. Flytzani-Stephanopoulos, *Appl. Catal. A: Gen.* 171 (1998) 13–29.
- [34] G. Avgouropoulos, T. Ioannides, *Appl. Catal. B: Environ.* 67 (2006) 1–11.
- [35] H.B. Zou, X.F. Dong, W.M. Lin, *Appl. Surf. Sci.* 253 (2006) 2893–2898.
- [36] E. Moretti, M. Lenarda, L. Storaro, A. Talon, T. Montanari, G. Busca, E. Rodríguez-Castellón, Antonio Jiménez-López, M. Turco, G. Bagnasco, R. Frattini, *Appl. Catal. A: Gen.* 335 (2008) 46–55.
- [37] P.F. Zhu, J. Li, S.F. Zuo, R.X. Zhou, *Appl. Surf. Sci.* 255 (2008) 2903–2909.
- [38] L. Qi, Q. Yu, Y. Dai, C.J. Tang, L.J. Liu, H.L. Zhang, F. Gao, L. Dong, Y. Chen, *Appl. Catal. B: Environ.* 119–120 (2012) 308–320.
- [39] B. Skárman, T. Nakayama, D. Grandjean, R.E. Benfield, E. Olsson, K. Niihara, L.R. Wallenberg, *Chem. Mater.* 14 (2002) 3686–3699.
- [40] B. Skárman, D. Grandjean, R.E. Benfield, A. Hinz, A. Andersson, L.R. Wallenberg, *J. Catal.* 211 (2002) 119–133.
- [41] S. Scirè, C. Crisafulli, P.M. Riccobene, G. Patanè, A. Pistone, *Appl. Catal. A: Gen.* 417–418 (2012) 66–75.
- [42] J.J. Luo, W. Chu, H.Y. Xu, C.F. Jiang, T. Zhang, *J. Nat. Gas Chem.* 19 (2010) 355–361.
- [43] Z.L. Wu, M.J. Li, S.H. Overbury, *J. Catal.* 285 (2012) 61–73.
- [44] J.Y. Kim, J.A. Rodriguez, J.C. Hanson, A.I. Frenkel, P.L. Lee, *J. Am. Chem. Soc.* 125 (2003) 10684–10692.
- [45] C.Q. Chen, Y.H. Zheng, Y.Y. Zhan, X.Y. Lin, Q. Zheng, K.M. Wei, *Cryst. Growth Des.* 8 (2008) 3549–3554.
- [46] T.X. Wang, S.H. Xu, F.X. Yang, *Powder Tech.* 228 (2012) 128–130.
- [47] B.G. Mishra, G.R. Rao, *J. Mol. Catal. A: Chem.* 243 (2006) 204–213.
- [48] K.N. Rao, P. Bharali, G. Thrimurthulu, B.M. Reddy, *Catal. Commun.* 11 (2010) 863–866.
- [49] Y.J. Kang, X.C. Ye, J. Chen, L. Qi, R.E. Diaz, V. Doan-Nguyen, G.Z. Xing, C.R. Kagan, J. Li, R.J. Gorte, E.A. Stach, C.B. Murray, *J. Am. Chem. Soc.* 135 (2013) 1499–1505.
- [50] W. Liu, M. Flytzani-Stephanopoulos, *J. Catal.* 153 (1995) 317–332.
- [51] S.H. Zeng, W.L. Zhang, S.L. Guo, H.Q. Su, *Catal. Commun.* 23 (2012) 62–66.
- [52] A. Gurbani, J.L. Ayastuy, M.P. González-Marcos, J.E. Herrero, J.M. Guil, M.A. Gutiérrez-Ortiz, *Int. J. Hydrogen Energy* 34 (2009) 547–553.